International Journal of Nanomedicine

Dovepress
Taylor & Francis Group

Open Access Full Text Article

ORIGINAL RESEARCH

Oxygen-Generating Biomimetic Nano-Herb System for Synergistic Therapy & Pain Relief in Triple-Negative Breast Cancer via HIF-1α/VEGF Pathway

Dian-Chao Cao[1–3,*], Yan Liang[1,4,*], Yang Guo[1], Dong-Yang Wu[1], Na-Na Wang[1], Yan-Mei Li[5], Hong-Fang Sun[1], Qin Wang[1], Xia Zhang[1], Yong-Liang Chi[6], Pei-Pei Sun[4], You-Jie Li[1], Ran-Ran Wang[7], Ping-Yu Wang[1,8], Shu-Yang Xie[1–3], Ning Xie[9]

[1]Department of Biochemistry and Molecular Biology, Binzhou Medical University, Yantai, Shandong, 264003, People's Republic of China; [2]Department of General Surgery, the second Medical College, Yantai Affiliated Hospital, Binzhou Medical University, Yantai, Shandong, 264003, People's Republic of China; [3]Shandong Laboratory of Advanced Materials and Green Manufacturing, Yantai, Shandong, 264000, People's Republic of China; [4]Department of Oncology, Binzhou Medical University Affiliated Hospital of Traditional Chinese Medicine, Binzhou, Shandong, 256600, People's Republic of China; [5]Department of Immune Rheumatism, Yantaishan Hospital, Yantai, Shandong, 264000, People's Republic of China; [6]Department of Anesthesiology, Affiliated Hospital of Shandong University of Traditional Chinese Medicine, Jinan, 250011, People's Republic of China; [7]Department of Rehabilitation Engineering, Institute of Rehabilitation Medicine, School of Rehabilitation Medicine, Binzhou Medical University, Yantai, Shandong, 264003, People's Republic of China; [8]Department of Epidemiology, Binzhou Medical University, Yantai, Shandong, 264003, People's Republic of China; [9]Department of Chest Surgery, Binzhou Medical University Affiliated Yantaishan Hospital, Yantai, Shandong, 264000, People's Republic of China

*These authors contributed equally to this work

Correspondence: Ning Xie, Department of Chest Surgery, Binzhou Medical University Affiliated Yantaishan Hospital, Yantai, Shandong, 264000, People's Republic of China, Tel +86-0535-6913211, Fax +86 0535 6913163, Email sunnyvvv@163.com; Shu-Yang Xie, Department of Biochemistry and Molecular Biology, Binzhou Medical University, Yantai, Shandong, 264003, People's Republic of China, Tel +86 0535 6913211, Fax +86 0535 6913163, Email xieshuyang@bzmc.edu.cn

Purpose: This study aims to develop an innovative delivery system, (Q+M/MnOx)@Clip, to enhance the bioavailability and therapeutic efficacy of quercetin both in tumor treatment and pain alleviation.

Methods: The (Q+M/MnOx)@Clip system was evaluated to enhance the release of quercetin, investigate its ability to target cancer cells, alleviate tumor hypoxia, and improve the efficacy of chemodynamic therapy (CDT). Tumor hypoxia markers and immune response activation were assessed, along with the impact on pain relief biomarkers.

Results: (Q+M/MnOx)@Clip successfully mitigated tumor hypoxia, facilitated controlled Q release, and enhanced CDT in vitro and in vivo. The system demonstrated a dual therapeutic effect: anti-tumor immunity and significant cancer pain relief by reducing HIF-1α and VEGF-A levels.

Conclusion: The novel (Q+M/MnOx)@Clip system represents a promising advancement in nanomedicine, improving the bioavailability of quercetin and offering a more effective approach to cancer treatment by downregulation of HIF-1α and VEGF-A. This study demonstrates the potential for combining anti-tumor immunity with pain relief for triple-negative breast cancer therapy.

Keywords: quercetin, pain relief, cancer immunotherapy, chemodynamic therapy, biomimetic, oxygen generation

Introduction

Breast cancer (BC) remains the most prevalent malignancy worldwide, posing a grave threat to women's health and well-being. Despite considerable progress in diagnostic and therapeutic modalities, BC continues to be the foremost contributor to cancer incidence and mortality among women, with annually escalating rates resulting in numerous fatalities.[1] Among the various BC subtypes, triple-negative breast cancer (TNBC) exhibits particular aggressiveness, heterogeneity, and drug resistance,[2] significantly narrowing the scope of treatment options.

Received: 26 February 2025
Accepted: 21 May 2025
Published: 31 May 2025

However, beyond the challenges posed by TNBC, another critical issue facing patients is cancer pain. A substantial proportion of late-stage cancer patients, ranging from 75% to 95%, endure significant pain, which drastically impairs their quality of life.[3] Cancer cells secrete pain mediators such as vascular endothelial growth factor (VEGF)-A, which sensitize and activate nociceptive receptors, thereby exacerbating the pain perception.[4] Notably, VEGF-A is intricately involved in both tumor angiogenesis and cancer pain, further compounding the complexities of treatment.

Quercetin (Q), with the molecular formula $C_{15}H_{10}O_7$, is a flavonoid compound widely found in traditional Chinese medicines, such as Sophora tonkinensis, Scutellaria baicalensis, and Sophora japonica flowers.[5] Q possesses antitumor properties and significant anti-nociceptive effects in diverse rodent models, simulating chronic pain that encompasses inflammatory, neuropathic, and cancer-induced pain.[6] Britti et al[7] discovered a remarkable reduction in VEGF-A expression levels in cancer cell lines following Q administration, indicating that it might be used as a supplementary therapy for suppressing cancer growth and alleviating cancer-related pain. Despite its promising properties, the clinical application of Q is hindered by several limitations, including its low water solubility, inadequate specificity for cancer targeting, and inefficient transport in the bloodstream following oral or intravenous administration.[8,9] Developing an intelligent delivery system to optimize the delivery efficiency of Q is urgently needed to overcome these challenges.

Therefore, in this study, we develop an oxygen-generating biomimetic nano-herb delivery system designated as (Q +M/MnOx)@Clip, which can overcome the challenges of Q application in vivo. As the herb delivery system described in previous studies,[10–12] we define the biomimetic nano-herb delivery system as a cell membrane-coated nanoparticle platform encapsulating standardized herbal-derived active compounds. This system was constructed by fusing the membrane of TNBC 4T1 cells for tumor targeting with a liposome membrane (Figure 1A). Natural melanin for induce immunogenic cell death (ICD) was synthesized with potassium permanganate through single-step biomineralization, resulting in the Melanin/MnOx (M/MnOx) hybrid. Q, for tumor suppression and pain relief, was encapsulated within the lipid bilayer of the nano-herb delivery system, and M/MnOx was integrated into its hydrophilic core. As illustrated in Figure 1B, (Q+M/MnOx)@Clip demonstrates exceptional targeting proficiency and herb delivery toward homologous cancer cells. Upon recognition and internalization by cancer cells, the nanodelivery system interacts with endogenous H_2O_2/H^+ to produce O_2. The oxygen generation induces internal pressure and oxidative stress, leading to the disruption of the biomimetic cancer cell membrane coating of the (Q+M/MnOx)@Clip nanocarrier. This disruption facilitates the subsequent release of MnOx and other therapeutic agents from the system. This process mitigates the hypoxic and acidic conditions within the immunosuppressive tumor microenvironment (TME) and rapidly triggers the rupture of the nanosystem within the cancer cells, thereby guaranteeing the effective release of the loaded drugs. This innovative system adeptly performs CDT and triggers DC activation while strengthening the immune system of the body, ultimately leading to cancer cell death. Furthermore, the T1-weighted imaging capability of (Q+M/MnOx)@Clip is conducive for innovative imaging-guided precision anti-cancer therapy. This system also significantly reduces VEGF-A levels, paving the way for the alleviation of cancer-related pain.

Materials and Methods

Materials

Melanin was isolated from the ink sac of a cuttlefish. High-purity Q (≥98%) and $KMnO_4$ were procured from Aladdin Chemical, Shanghai, China. H&E Staining Kit, Reactive Oxygen Species (ROS) Assay Kit, Mouse Splenic Lymphocyte Isolation Kit, and Bicinchoninic Acid (BCA) Protein Assay Kit were procured from Solaibao Biological Technology Co., Ltd. Dil Kit (red fluorescence) and DiO Kit (green fluorescence), specifically designed for staining the cell plasma membrane, and Membrane and Cytosol Protein Extraction Kit were sourced from Biyuntian Biotechnology, Shanghai, China.

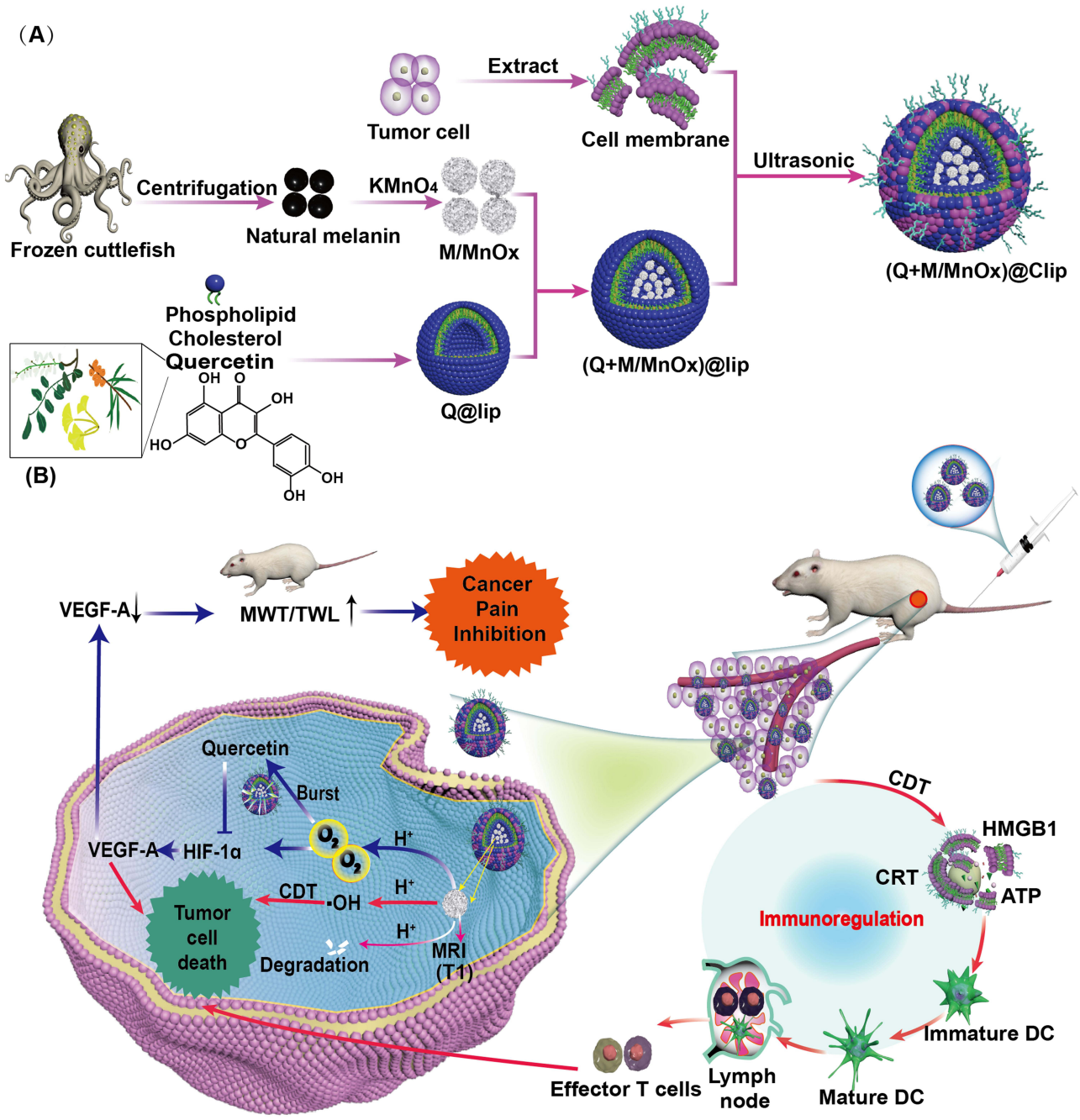

Figure 1 Schematic illustration of this system. (**A**) Synthesis diagram of oxygen-producing biomimetic nano-herb delivery system ((Q+M/MnOx)@Clip). (**B**) Schematic of (Q+M/MnOx)@Clip for potentiated cancer therapy and pain mitigation in vivo.

Fabrication and Characterization of the Prepared nanomaterials

Fabrication of M/MnOx Hybrids

M/MnOx hybrids were synthesized by single-step biomineralization.[13] The melanin nanoparticles MNPs (6.45 mg) dispersed in 15 mL of water were sonicated and then slowly added with $KMnO_4$ (10 mL, 3 mg/mL) under stirring at 350 rpm. Finally, M/MnOx hybrids were obtained after 5 min of stirring and centrifugation at 8000 rpm for 10 min.

Fabrication of (Q+M/MnOx)@lip

(Q+M/MnOx)@lip was prepared via thin-film hydration.[14] Cholesterol (9.5 mg), phospholipid (36.1 mg), and Q (4.5 mg) were dissolved in chloroform. After vacuum evaporation at 40 °C, the membrane was hydrated with M/MnOx and

https://doi.org/10.2147/IJN.S523754

ultrasonicated with a 200 w probe every 10 min to obtain (Q+M/MnOx)@lip. The same method was used to synthesize the other liposomes.

Fabrication of (Q+M/MnOx)@Clip

In brief, 1 mL of the prefabricated (Q+M/MnOx)@lip was transferred to a 2.0 mL EP tube containing tumor cell membrane (cell membrane to liposome ratio 1:1), and the mixture was further sonicated for 3 min. Unbound cancer cell membrane was eliminated via centrifugation, followed by two washes with PBS, yielding (Q+M/MnOx)@Clip.[15]

Characterization of (Q+M/MnOx)@Clip

The particle size, polydispersion index (PDI), and zeta potential of the nanoparticles were investigated by dynamic light scattering (DLS). Morphologies were examined by transmission electron microscopy, and elemental mapping was analyzed using the energy dispersive spectrometer (EDS) of the TEM apparatus. The elemental composition of (Q+M/MnOx)@Clip and the valences of Mn ions were analyzed by X-ray photoelectron spectroscopy (XPS) and high-resolution XPS.

The stability of (Q+M/MnOx)@Clip was determined in RPMI medium containing 10% fetal bovine serum (FBS). For the assessment of its degradation efficacy, (Q+M/MnOx)@Clip was incubated in a buffer solution under varying conditions for 12 h. Its in vivo degradation safety was monitored via TEM.

In vitro Drug Release Properties

A solution of 2 mL (Q+M/MnOx)@Clip, quantified with Q at 0.45 mg/mL, was sealed in dialysis bags (MWCO = 1,000 Da) to mimic in vitro Q release across varying pH levels. At each time point, 1 mL of dialysate was collected for quantification and replenished with an equal volume of fresh dialysate. Q concentrations were determined using UV-vis spectrophotometry.[16,17]

Detection of O_2 and Extracellular $^{\cdot}OH$ Production

The oxygen-generating capacity of (Q+M/MnOx)@Clip in diverse solutions was rigorously assessed by utilizing a portable dissolved oxygen meter. The production of extracellular •OH radicals during CDT was confirmed through the degradation of methylene blue (MB).[18]

Cell Culture

For cell culture studies, mouse breast cancer 4T1, human colorectal adenocarcinoma SW480, mouse melanoma B16, mouse fibroblasts L929 cells, and human breast cancer MDA-MB-231 cell lines were purchased from the Shanghai Institute of Cell Biology, Chinese Academy of Sciences, China. The 4T1, SW480, B16, and L929 cells were grown in RPMI-1640 medium sustained at 37 °C in a 5% CO_2 atmosphere. Meanwhile, MDA-MB-231 cells were cultured in DMEM medium under similar temperature and conditions.

In vitro Biocompatibility and Cytotoxicity Assays

M/MnOx, Q@lip, (Q+M/MnOx)@lip, and (Q+M/MnOx)@Clip were separately incubated with 4T1 cells. After 24 h of coculture, MTT assay, live–dead staining, and apoptosis detection were performed to evaluate the antitumor effects.

Intracellular O_2 Production and Hypoxia-Inducible Factor-1α(HIF-1α)/VEGF-A Expression

Intracellular O_2 production levels were investigated using an Oxidative Stress/Hypoxia Detection Kit to evaluate the ability of (Q+M/MnOx)@Clip to alleviate hypoxia in 4T1 cells.[13] ROS levels were measured using a ROS Assay Kit. HIF-1α expression in 4T1 cells cultured with different nanoparticles for 24 h was investigated by immunofluorescence staining. VEGF-A levels in the cell supernatant were detected by ELISA in accordance with the manufacturer instructions. Furthermore, proteins were extracted from the cocultured cells for Western blot (WB) analysis.

In vitro Induction of ICD

M/MnOx, Q@lip, (Q+M/MnOx)@lip, and (Q+M/MnOx)@Clip were co-incubated with 4T1 cells for 24 h. High mobility group box-1 protein (HMGB1) in the cell supernatant was detected using an HMGB1 ELISA Kit, and the ATP levels in supernatant were detected with a chemiluminescence ATP Assay Kit. The surface localization of calreticulin (CRT) was visualized using immunofluorescence.[19]

Animal Experiments

Five-week-old female BALB/c mice were purchased from Hangzhou Ziyuan Laboratory Animal Technology Co., Ltd. (Hangzhou, China). A murine cancer pain model was established by injecting 10×10^4 4T1 cells into muscle tissue adjacent to a 0.5 cm open nerve adjacent to the hip joint. At 7 days after inoculation, the tumor diameter reached 4–6 mm, indicating that the mouse model of breast cancer pain was successfully established.[20,21]

Animal experimentation was conducted in accordance with the rigorous guidelines established by the National Institute of Health for the Care and Utilization of Laboratory Animals in China while ensuring full adherence to the ethical standards and regulations outlined by the Administrative Committee for Experimental Animals at Binzhou Medical University (No. 2023–02-02, Yantai, China).

Animal Imaging Experiments and T1-MR Images

The safety of (Q+M/MnOx)@Clip for intravenous administration was investigated by hemolysis test. The IVIS spectrum in vivo small animal imaging system (PerkinElmer, USA) was utilized to observe tissue accumulation at various time points subsequent to the intravenous administration of diverse formulations. T1-weighted imaging was employed to assess the in vivo and ex vivo MR imaging capability of (Q+M/MnOx)@Clip.

In vivo Antitumor Efficacy

Healthy female BALB/c mice aged 5–6 weeks were selected for the establishment of a breast cancer-induced pain model. Once the tumor size reached 100 mm^3, 25 BALB/c mice were randomly assigned to five groups: PBS, Q@lip, M/MnOx, (Q+M/MnOx)@lip, and (Q+M/MnOx)@Clip. Each group received intravenous injections, and the tumor volumes and mouse weights were recorded every other day throughout a 14-day treatment period. Following treatment, all major organs including the heart, liver, spleen, lungs, and kidneys and tumor tissues were harvested and subjected to H&E staining. For further investigation on the immune response during tumor therapy, lymph nodes, spleen, and adjacent tumor tissues were resected 14 days after treatment and used to test the ability of nanoparticles to promote DC maturation in vivo. In addition, the $CD4^+$ T and $CD8^+$ T lymphocytes in the spleen were detected.

In vivo Ability to Relieve Cancer Pain

The mechanical withdrawal threshold (MWT) and thermal withdrawal latency (TWL) were measured to thoroughly investigate the analgesic efficacy of each group. Furthermore, immunohistochemistry (IHC) and WB techniques were employed to detect the in vivo expression levels of HIF-1α and VEGF-A, providing valuable insights into the underlying mechanisms.

Statistical Analysis

SPSS 22.0 software (IBM Corp., Armonk, NY, USA) was utilizing for all statistical computations. Averages and multiple groups were analyzed by student's *t* test and ANOVA. ns $P > 0.05$, $^*P < 0.05$, $^{**}P < 0.01$, $^{***}P < 0.001$ were considered statistically significant.

Results

Characterization of the Prepared Nanomaterials

MNP served as a bionic template to reduce $KMnO_4$, yielding monodisperse M/MnOx hybrid (~221.7 nm, Figure 2A) via single-step biomineralization. The TEM image of M/MnOx hybrids displayed spherical, rough surfaces free of large

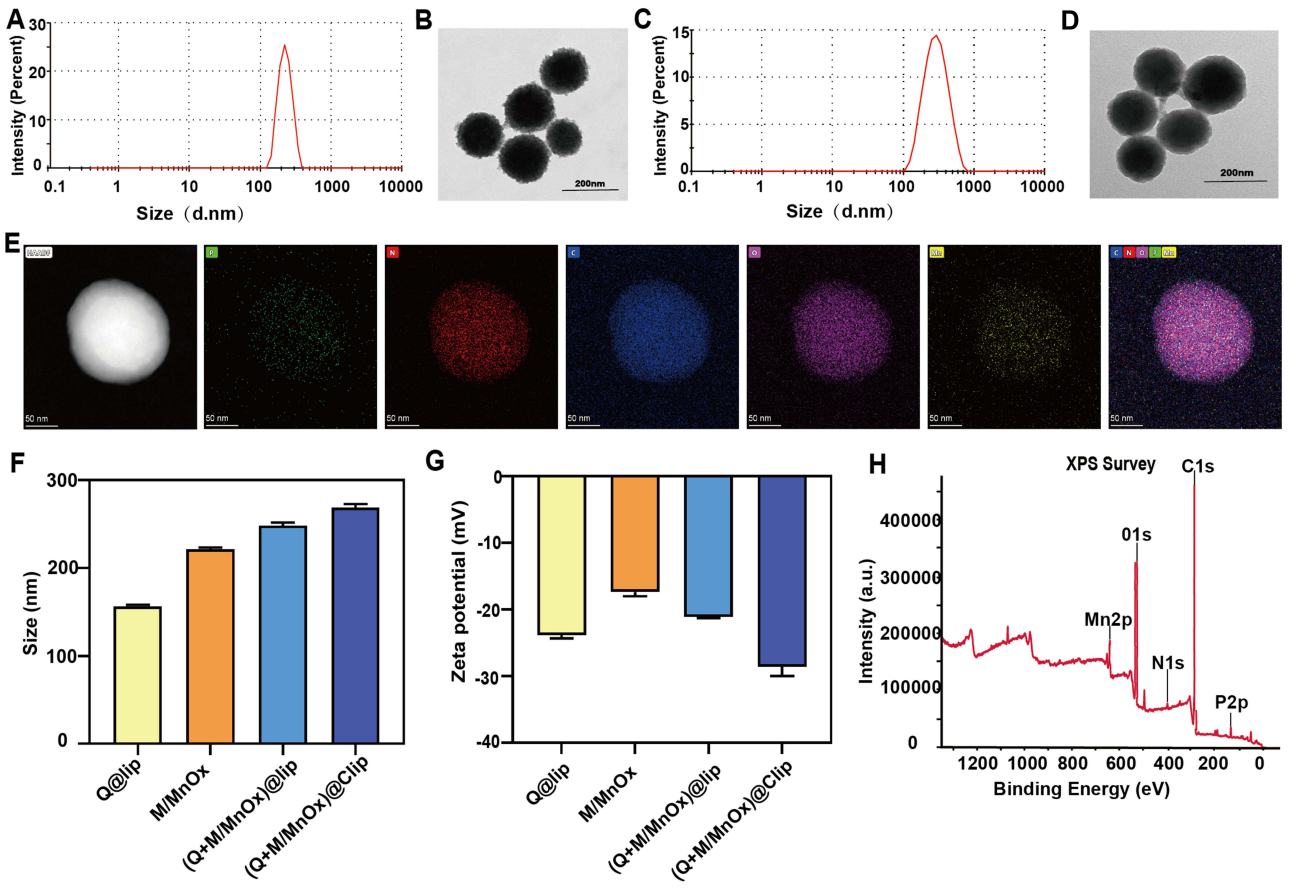

Figure 2 The characterization of the nano-herb delivery system. **(A)** Particle size distribution and (**B**) TEM of M/MnOx hybrids. (**C**) Particle size distribution and (**D**) TEM of (Q+M/MnOx)@Clip (bar = 200 nm). (**E**) Elemental mapping of (Q+M/MnOx)@Clip (bar = 50 nm). Columnar chart of (**F**) the particle size and (**G**) potential diagram of four different nanoformulations. (**H**) Representative XPS spectra of (Q+M/MnOx)@Clip.

agglomeration (Figure 2B). Well-dispersed (Q+M/MnOx)@Clip nanoparticles with approximately 270 nm size were formed as illustrated in Figure 2C. TEM images revealed their spherical shape and smooth surface (Figure 2D), and TEM element mapping demonstrated the uniform distribution of phosphorus, carbon, nitrogen, oxygen, and manganese within the (Q+M/MnOx)@Clip nanoparticles (Figure 2E). DLS quantified the particle sizes of Q@lip, M/MnOx, (Q+M/MnOx)@lip, and (Q+M/MnOx)@Clip nanoparticles to be 156.5 ± 1.604, 221.7 ± 1.801, 248.5 ± 3.460, and 268.8 ± 4.244 nm, respectively (Figure 2F). Their PDI in solution is presented in Figure S1A, reflecting the uniformity and colloidal stability of the formulated nanoparticles in solution. This homogeneous particle dispersion is essential for ensuring the consistent drug delivery performance and enhanced tumor targeting efficiency. The observed increase in particle size could be attributed to the effective incorporation of M/MnOx and cancer cell membranes, underscoring the successful synthesis and modification of the nanoparticles. In addition, the zeta potentials of Q@lip, M/MnOx, (Q+M/MnOx)@lip, and (Q+M/MnOx)@Clip were −23.82 ± 0.511, −17.37 ± 0.635, −21.13 ± 0.153, and −28.57 ± 1.405 mV, respectively (Figure 2G). XPS analysis confirmed the presence of phosphorus, carbon, nitrogen, oxygen, and manganese elements within (Q+M/MnOx)@Clip (Figure 2H). The high-resolution XPS spectra of Mn2p3/2 unambiguously revealed the coexistence of Mn^{2+}, Mn^{3+}, and Mn^{4+} valence states within the M/MnOx nanohybrid materials as shown in Figure S1B. This finding underscores the complexity and versatility of the nanomaterials' composition.

The protein profiles of cancer cells, cancer cell membranes, and (Q+M/MnOx)@Clip were analyzed by SDS-PAGE. As shown in Figure 3A, the fused (Q+M/MnOx)@Clip hybrid membrane nanomaterials retained the proteins of 4T1 breast cancer cell membranes, indicating that (Q+M/MnOx)@lip and 4T1 cancer cell membranes were successfully fused. CD44, the ubiquitous membrane glycoprotein, is prominently expressed across a diverse spectrum of cancerous cells.[22] WB analysis was performed for the membrane-specific CD44 protein markers of (Q+M/MnOx)@Clip

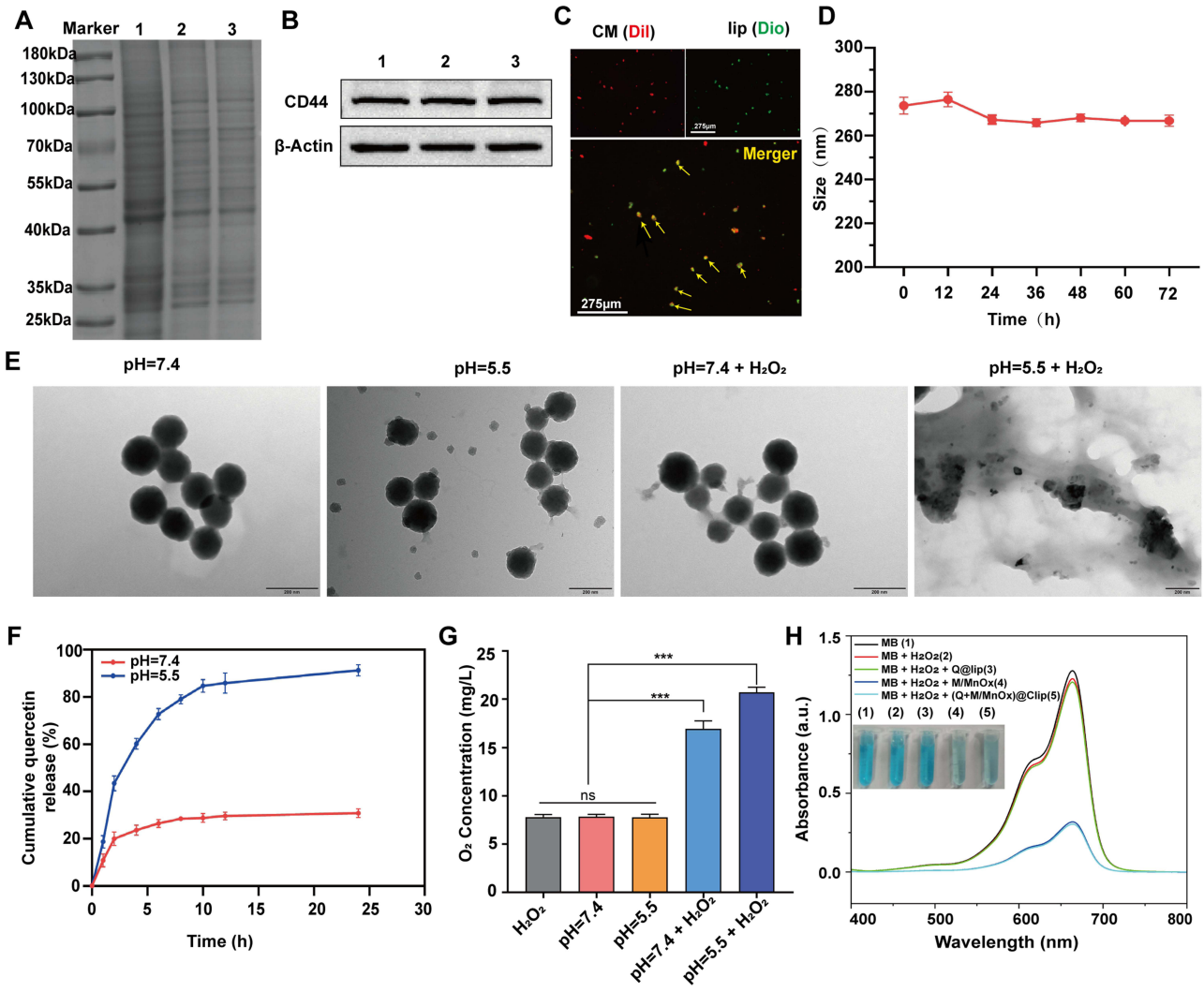

Figure 3 The analysis of protein and stability of this system. (**A**) SDS-PAGE analysis of protein components (Group-1 stands for 4T1 cells, 2 stands for 4T1 cell membrane, and 3 stands for (Q+M/MnOx)@Clip). (**B**) WB analysis for CD44, markers of membrane marker protein (lane 1, 4T1 cells; lane 2, 4T1 cell membrane; lane 3, (Q+M/MnOx)@Clip). (**C**) Representative photomicrograph of the cofusion of cell membrane (CM) and liposome membrane labeled with red (DiI) and green (DiO) fluorescent dyes (bar = 275 μm). (**D**) Time-dependent colloidal stability of (Q+M/MnOx)@Clip. (**E**) TEM images of (Q+M/MnOx)@Clip treated in different pH solutions (bar = 200 nm). (**F**) Cumulative release percentage of quercetin over time. (**G**) Oxygen-producing capability of (Q+M/MnOx)@Clip under different conditions(mean ± SD, n = 3, ns, $P > 0.05$, ***, $P < 0.001$). (**H**) UV-vis absorption spectra and photo (inset) after MB degradation at different solutions.

(Figure 3B). Upon examination under a fluorescence microscope, the cancer cell membrane was confirmed to be incorporated into the (Q+M/MnOx)@lip nanomaterials (Figure 3C). The tagged (Q+M/MnOx)@lip was then blended with the tagged cancer cell membrane, followed by the application of ultrasound for effective integration. Analysis of the resultant (Q+M/MnOx)@Clip nanomaterial revealed a pronounced colocalization of the fluorescence signals, yielding a distinct yellow hue (Figure 3C) confirming the successful integration.

Furthermore, (Q+M/MnOx)@Clip maintained a relatively consistent hydrodynamic size throughout a 3-day incubation period in a medium containing 10% fetal bovine serum, underscoring its remarkable serum stability within a physiological environment (Figure 3D). This finding attested to the potential of (Q+M/MnOx)@Clip for stability in vivo.

In vitro Characterization of (Q+M/MnOx)@Clip

The TME is distinctly marked by hypoxia, abundant H_2O_2 concentrations of up to 100 μM, and an acidic pH.[23] Given the biodegradability of (Q+M/MnOx)@Clip within challenging environments, its degradation patterns were systematically

https://doi.org/10.2147/IJN.S523754

assessed across various buffer systems. (Q+M/MnOx)@Clip exhibited pronounced degradation exclusively in acidic buffers fortified with H_2O_2, indicative of its responsiveness to the characteristic conditions of the TME. When exposed to neutral, purely acidic, or hydrogen peroxide-only conditions, the morphology of (Q+M/MnOx)@Clip remained largely unchanged (Figure 3E), affirming its capacity for selective degradation specifically triggered by the distinctive chemistry of the TME.

A solution containing 0.4 mg/mL of the formulation (quantified in terms of M/MnOx content) was dispersed in PBS at two distinct pH levels, 7.4 and 5.5, to assess the pH-responsive drug release characteristics of (Q+M/MnOx)@Clip. These dispersions were subjected to agitation at 100 rpm and maintained at 37 °C to mimic physiological conditions. The release profiles of Q, the active ingredient, at these varying pH values were quantitatively by UV-vis spectroscopy (Figure 3F). At pH 5.5, the cumulative release of Q from (Q+M/MnOx)@Clip was markedly elevated compared with its release at pH 7.4. This pronounced enhancement can be rationalized by the ability of M/MnOx to accelerate the catalytic rate under acidic conditions. In particular, the enhanced catalytic activity of M/MnOx at low pH leads to the generation of a copious amount of O_2, which subsequently disrupts the integrity of the liposomes and thereby facilitates the expedited release of Q.

We conducted a series of experiments to further understand the O_2-generating potential of (Q+M/MnOx)@Clip within the intricate TME. As shown in Figure 3G, (Q+M/MnOx)@Clip demonstrated remarkable efficacy in catalyzing H_2O_2 decomposition (at a concentration of 100 μM), thereby generating O_2, which holds significant promise for alleviating the hypoxic conditions prevalent in tumor tissues.

To evaluate the extracellular •OH production catalyzed by (Q+M/MnOx)@Clip, we utilized a MB degradation assay as a precise indicator for the direct monitoring of •OH generation throughout CDT.[24] In particular, UV-vis spectrophotometer was used to track alterations in the characteristic absorption peak of MB, providing a reliable indication of •OH activity. •OH production was quantified by observing a distinct decrease in the UV absorption peak intensity of MB as shown in Figure 3H, thereby confirming the efficacy of (Q+M/MnOx)@Clip in catalyzing •OH generation.

In vitro Cellular Uptake and Homologous Targeting

The efficient internalization of nanomaterials by tumor cells holds paramount significance in inhibiting tumor growth.[25] To delve into the targeting proficiency of cell membrane fusion nanoparticles toward tumor cells, we conducted an experiment utilizing (Q+M/MnOx)@lip and (Q+M/MnOx)@Clip, both labeled with the green fluorescent dye FITC. At every time point examined, the (Q+M/MnOx)@Clip group exhibited a strikingly higher cellular fluorescence intensity than the (Q+M/MnOx)@lip group (Figure 4A). This finding underscored the efficacy of biomimetic liposomes in facilitating and enhancing the uptake by tumor cells.

After coculturing a uniform concentration of FITC-labeled (Q+M/MnOx)@Clip with various cell lines containing an equal number of cells for 4 h, we employed FCM to quantify the fluorescence intensity within each cell line. The findings revealed a conspicuously heightened uptake of (Q+M/MnOx)@Clip by the homologous 4T1 cells compared with that by the heterologous cells (Figure 4B and C), which indicated that this system can selectively recognize and interact with cells of the same tumor sources. Although the fluorescence peaks of B16 and 4T1 cells appeared similar in flow cytometry (Figure 4B), which may be attributed to their comparable endocytic capacities. Nevertheless, quantitative analysis confirmed that 4T1 cells exhibited significantly higher mean fluorescence intensity (Figure 4C).

In vitro Biocompatibility and Cytotoxicity Assays

The antitumor property of varied nanomaterials was examined in a controlled in vitro setting. As an initial step, we employed the MTT assay to quantify the suppression of cell proliferation (Figure 4D). (Q+M/MnOx)@lip exhibited a superior inhibitory effect on 4T1 cell viability, markedly outperforming its M/MnOx and Q@lip counterparts. This exceptional performance underscored the profound synergy achieved by the combined M/MnOx and Q, surpassing the limitations of standalone therapies and showcasing a remarkable enhancement in antitumor efficacy. Furthermore, the cellular toxicity of (Q+M/MnOx)@Clip was elevated compared with that of (Q+M/MnOx)@lip. This disparity could be attributed to the enhanced cellular uptake capabilities of the biomimetic liposomes.

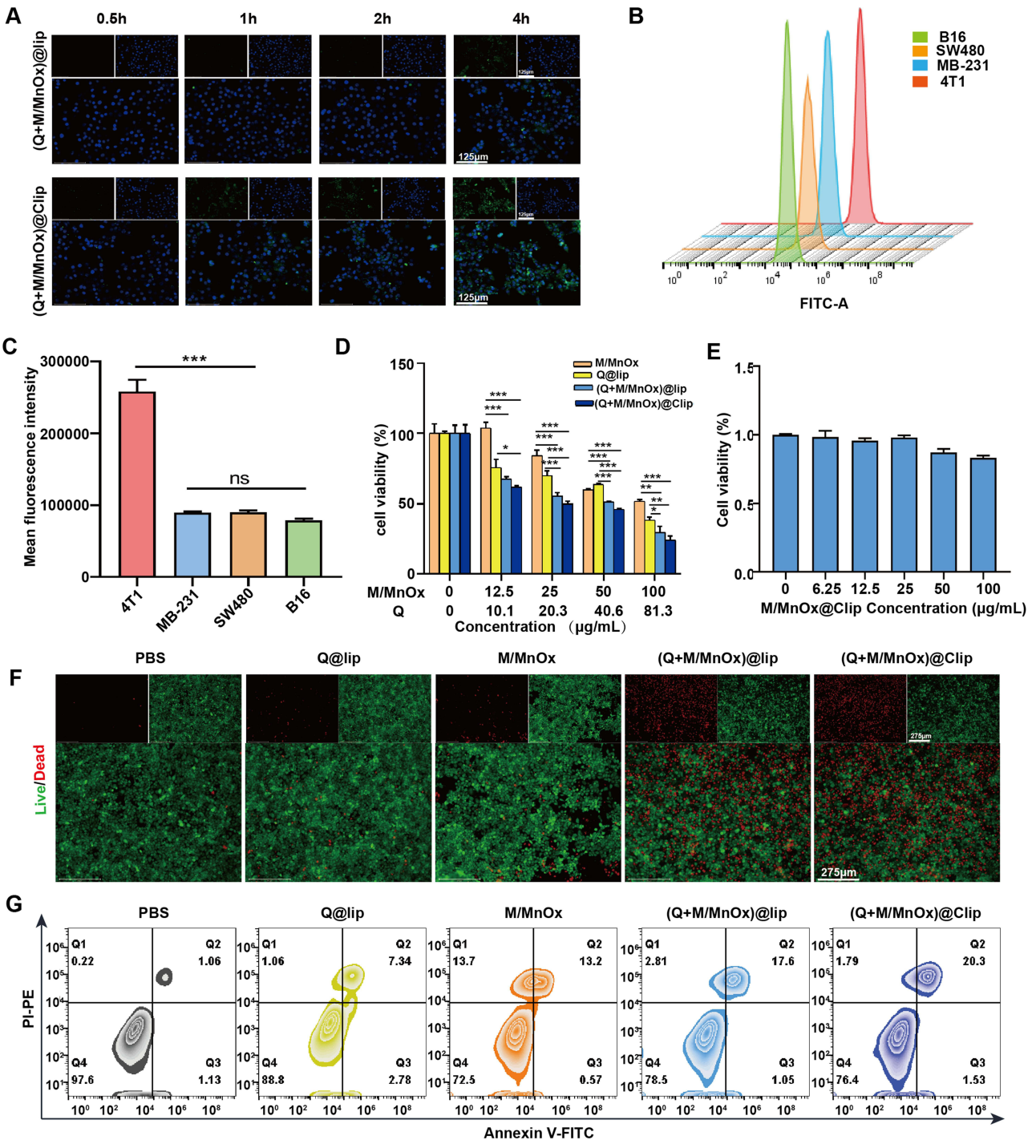

Figure 4 The cellular uptake and effects of nanoparticles on tumor cells. (**A**) In vitro cellular uptake and internalization of fluorescent nanoparticles with and without the cell membrane fusion at different lengths of time (bar = 125 μm). (**B**) Homologous targeting of (Q+M/MnOx)@Clip for different cells analyzed by FCM and (**C**) corresponding quantitative analysis. (**D**) Cytotoxicity and (**E**) cytocompatibility determined by MTT. (**F**) Live/dead images of different formulations (green-live, red-dead) (bar = 275 μm). (**G**) FCM analysis of cell apoptosis. (mean ± SD, n = 3, ns, $P > 0.05$, *, $P < 0.05$, **, $P < 0.01$, ***, $P < 0.001$).

To assess the biosafety of nanocarriers, the results showed that, even at a concentration of 100 μg/mL, M/MnOx@Clip maintained a cell viability of approximately 80%, demonstrating its exceptional biocompatibility and safety profile (Figure 4E).

The responsive degradation of M/MnOx within the acidic TME triggers O_2 generation, effectively rupturing the biomimetic fusion membrane of the nanoparticles. This process liberates Mn^{2+}, which subsequently generate •OH

https://doi.org/10.2147/IJN.S523754

radicals, potentiating the cytotoxic effects against tumor cells. To visually substantiate these findings, the live/dead cell assays results revealed a pronounced increase in red fluorescence, indicative of dead cells, in the (Q+M/MnOx)@Clip treatment group compared with that in the controls. This compelling evidence underscored the remarkable anti-tumor efficacy of (Q+M/MnOx)@Clip as illustrated in Figure 4F.

The apoptotic analyses reveal distinct differences in the apoptosis rates, with PBS demonstrating the lowest rate at approximately 2.387%, followed by Q@lip at 9.553%, M/MnOx at 14.96%, (Q+M/MnOx)@lip at 19.14%, and the highest rate was observed in the (Q+M/MnOx)@Clip group at 22.15% (Figure 4G and Figure S2). This pattern of increasing apoptosis rates aligns perfectly with the trends observed in the MTT assays and live/dead cell determinations, reinforcing the effectiveness of (Q+M/MnOx)@Clip in inducing cell death.

Anti-Tumor Mechanism of (Q+M/MnOx)@Clip in vitro

The hypoxia within the TME is important for tumor procession,[26] and Q was reported to effectively inhibit tumor growth and metastasis by suppressing HIF-1α/VEGF-A pathway.[25] Thereafter, the hypoxia alleviation, VEGF-A expression and immune system activation were investigated after 4T1 cells were treated with the nanoparticles. The intracellular hypoxia status results displays a pronounced reduction in red fluorescence intensity in the 4T1 cells co-incubated with (Q+M/MnOx)@Clip, which is in stark contrast with that observed in the PBS-treated group (Figure 5A). This finding underscored the impact of (Q+M/MnOx)@Clip on alleviating hypoxia in the targeted cells. The expression level of HIF-1α, a pivotal marker of cellular hypoxia response, also exhibited a downward trend as illustrated in Figure 5B. The diminished expression of HIF-1α subsequently led to the downregulation of VEGF-A, a downstream effector, ultimately inhibiting the production and release of VEGF-A within tumor cells (Figure 5C and D). ROS generation in the 4T1 cells was quantitatively assessed by utilizing a DCFH-DA probe, with the emergence of green fluorescence serving as an indicator of ROS presence. The 4T1 cells subjected to (Q+M/MnOx)@Clip exhibited pronounced green fluorescence (Figure S3), suggesting an enhancement in ROS production possibly mediated by M/MnOx. The generation of toxic •OH amidst the ROS surge imparted the capability to induce cytotoxic effects on tumor cells, ultimately prompting ICD and stimulating an antitumor immune response.[27]

We next investigated the ICD to evaluate the anti-tumor immune response. The damage-associated molecular patterns (DAMPs), encompassing HMGB1, ATP, and CRT, promote DC maturation and antigen presentation. Compared with that in the PBS control group, a notable augmentation in the secretion of HMGB1, ATP, and CRT was observed across all the treated 4T1 cells, albeit to varying degrees (Figure 5E–G). The (Q+M/MnOx)@Clip nanoformulation stood out, eliciting the most pronounced release of HMGB1 and ATP the most distinct exposure of CRT on the surface of the 4T1 cells. This finding underscored the efficacy of the (Q+M/MnOx)@Clip in enhancing ICD pathways.

DAMPs and tumor-associated antigens (TAAs) could potently enhance DC maturation.[28] The results further showed that (Q+M/MnOx)@Clip group demonstrated substantial enhancement in DC maturation, surpassing that in the untreated 4T1 control (Figures 5H and S4). This discovery highlighted the capacity of (Q+M/MnOx)@Clip to capitalize on DAMP-elicited signals, thereby propelling DC maturation.

In vivo Biodistribution Analyses

The blood compatibility of intravenous delivery is crucial for biocompatibility assessment.[29] As depicted in Figure S5A and B, the (Q+M/MnOx)@Clip group exhibited a hemolysis rate of less than 5% even at a high concentration of 600 μg/mL, underscoring its exceptional blood compatibility and promising potential for intravenous administration.

(Q+M/MnOx)@lip and (Q+M/MnOx)@Clip were fluorescently tagged with Cy5.5 (Figure S6A and B) and intravenously injected in the mouse model of cancer pain at identical doses. The distribution and accumulation of nanoparticles specifically within the tumor sites were then monitored to assess their targeted delivery efficiency. In the initial 4 h, minimal differences were discernible between the (Q+M/MnOx)@lip and (Q+M/MnOx)@Clip groups. However, at the 12-hour mark, a marked increase in fluorescence intensity was observed for the (Q+M/MnOx)@Clip group, surpassing that of the (Q+M/MnOx)@lip group and achieving peak accumulation (Figure 6A), which underscored the capability of biomimetic hybrid membrane-coated nanoparticles to harness homologous tumor targeting. At 48 h post-injection, tumor tissue and vital organs (heart, liver, spleen, lung, and kidney) were excised for imaging to assess the systemic distribution

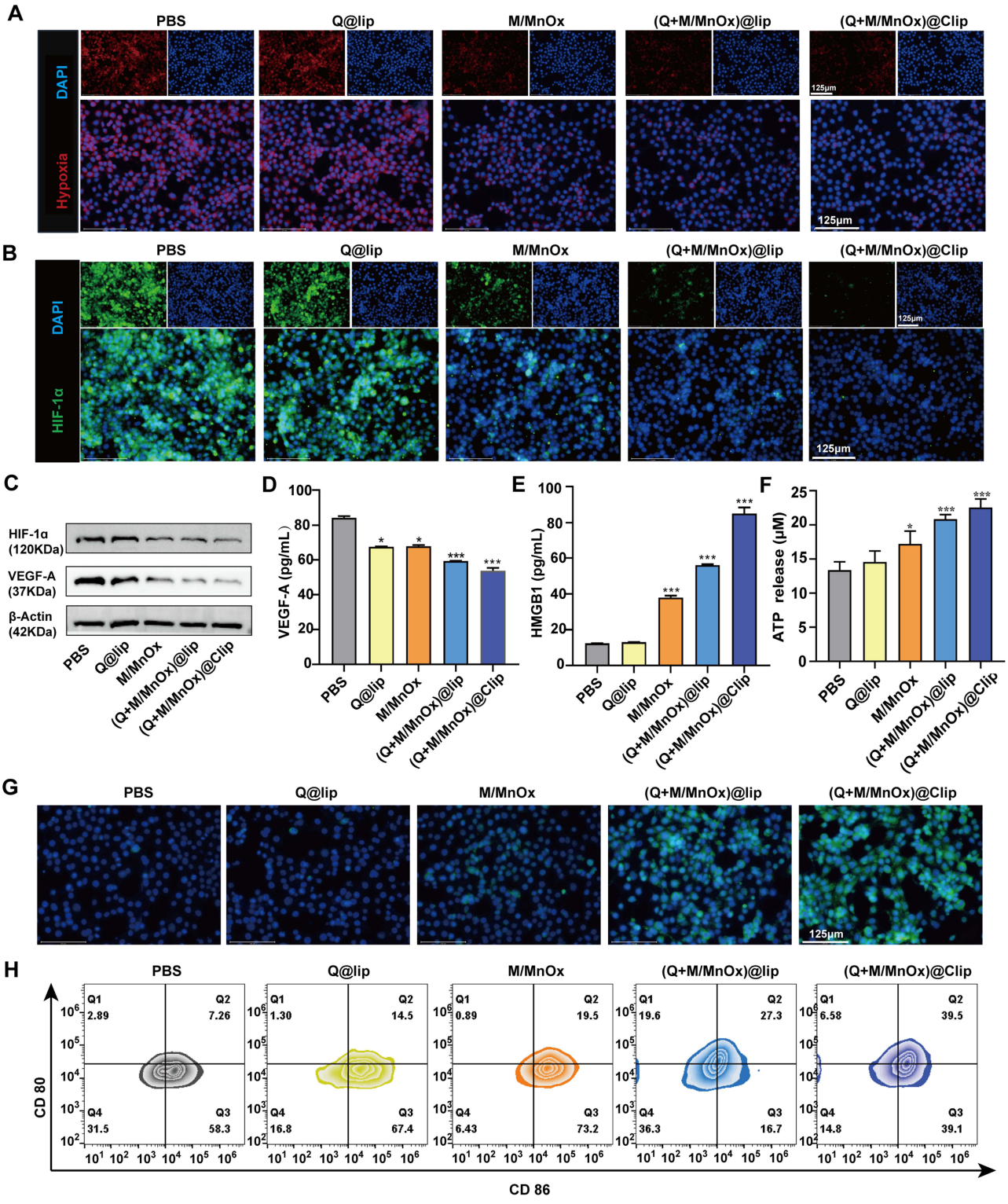

Figure 5 The system induced the hypoxia alleviation and anti-tumor immune. (**A**) Intracellular hypoxia status after different treatments was detected by fluorescence microscopy after the cells were stained by the intracellular hypoxia reagent (bar = 125 μm). (**B**) HIF-1α levels were detected by immunofluorescence (bar = 125 μm). (**C**) HIF-1α and VEGF-A expression levels were analyzed by WB. (**D**) VEGF-A in cell supernatants was quantified by ELISA. (**E**) HMGB1 release in supernatant was analyzed by ELISA. (**F**) ATP content was determined with ATP Assay Kit. (**G**) Representative immunofluorescence staining images of CRT expression (green) on the surface of 4T1 cells after various treatments (bar = 125 μm). (**H**) DC maturation markers (CD80 and CD86) were assessed using FCM. (mean ± SD, n = 3, *, $P < 0.05$, ***, $P < 0.001$).

https://doi.org/10.2147/IJN.S523754

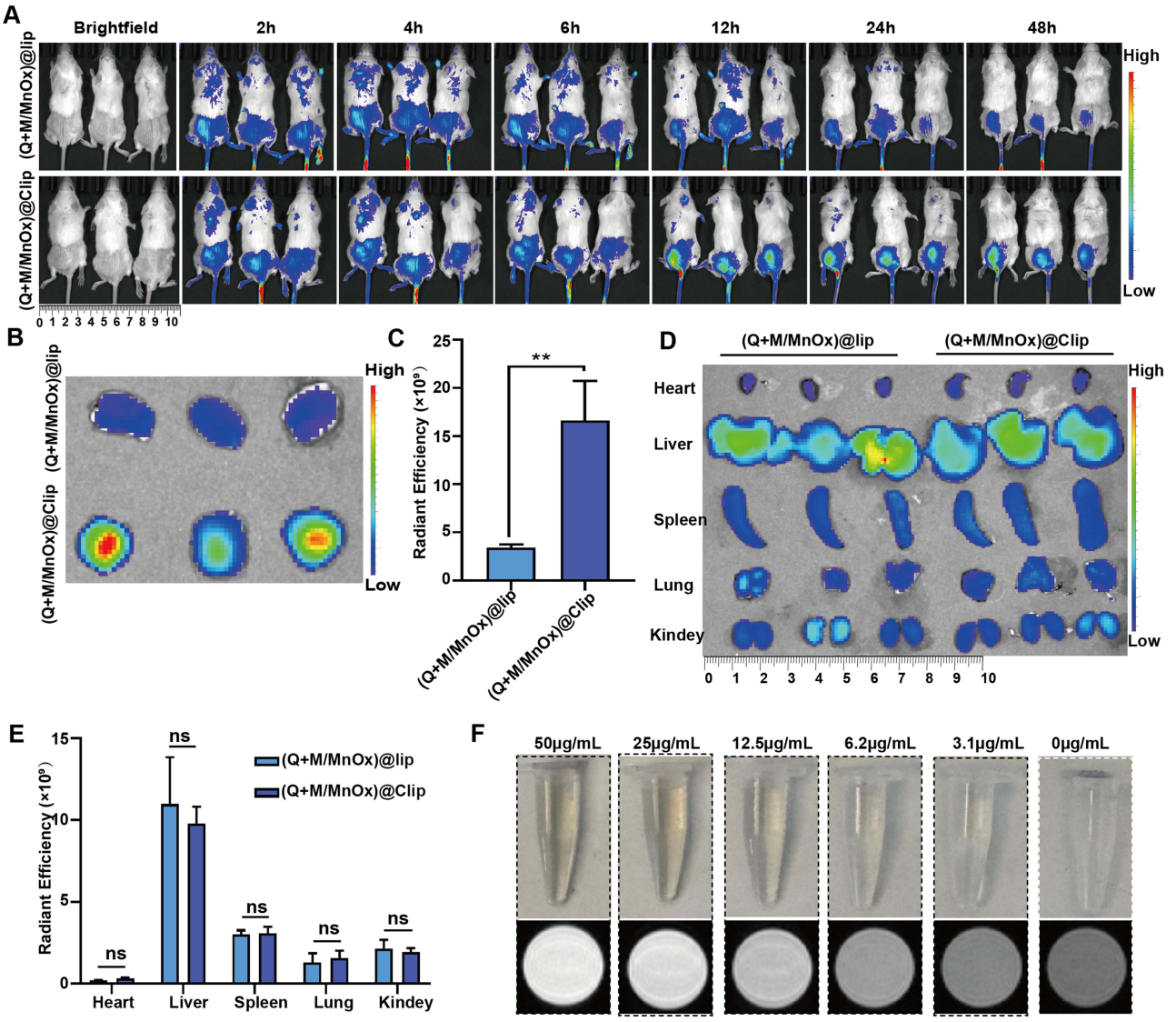

Figure 6 The biodistribution analyses of nanoparticles. (**A**) Tissue distributions of (Q+M/MnOx)@lip and (Q+M/MnOx)@Clip at indicated time points following i.v. (n = 3). (**B**) Ex vivo fluorescence imaging and (**C**) quantification of tumors at 48 h after intravenous injection (mean ± SD, n = 3, **, $P < 0.01$). (**D**) Ex vivo fluorescence imaging and (**E**) quantification of different organs (heart, liver, spleen, lung, and kidney) at 48 h after intravenous injection (mean ± SD, n = 3, ns, $P > 0.05$). (**F**) In vitro T1-weighted MRI images of (Q+M/MnOx)@Clip at different concentrations.

of the nanoparticles. Ex vivo tumor fluorescence revealed a higher fluorescence intensity in the (Q+M/MnOx)@Clip group than in the (Q+M/MnOx)@lip group (Figure 6B and C). (Q+M/MnOx)@Clip demonstrated exceptional targeting specificity and accumulation efficiency, primarily attributed to its biomimetic membrane coating that facilitated effective accumulation within the tumor tissue. No discernible differences were observed in the distribution patterns of (Q+M/MnOx)@lip and (Q+M/MnOx)@Clip within the heart, liver, spleen, lung, and kidneys (Figure 6D–E). In vitro T1-weighted magnetic resonance imaging (MRI) images of (Q+M/MnOx)@Clip at varying concentrations and T1-weighted MRI scans in tumor-bearing mice confirmed the MRI capability of (Q+M/MnOx)@Clip as exemplified in Figure 6F and Figure S6C and D. Specifically, Figure 6F presents the in vitro T1-weighted MRI images of (Q+M/MnOx)@Clip at different concentrations, showing a concentration-dependent enhancement in MRI signal intensity. This enhancement is attributed to the increased Mn ion content at higher nanoparticle concentrations, which effectively shortens the longitudinal relaxation time (T1), thereby improving the T1-weighted MRI contrast. These results collectively demonstrate that the (Q+M/MnOx)@Clip may act as an effective T1 contrast agent with concentration-dependent imaging capability.

In vivo Antitumor Effects of (Q+M/MnOx)@Clip

To explore the anti-cancer and analgesic effects of (Q+M/Mnox)@Clip in vivo, we conducted in vivo tumor treatment following the standard experimental protocol (Figure 7A). As illustrated in Figure 7B, the (Q+M/MnOx)@Clip group displayed the most pronounced inhibition of tumor growth, significantly surpassing that observed in the PBS, Q@lip, M/MnOx, and (Q+M/MnOx)@lip groups. This result underscored the superior efficacy of the (Q+M/MnOx)@Clip in suppressing tumor proliferation.

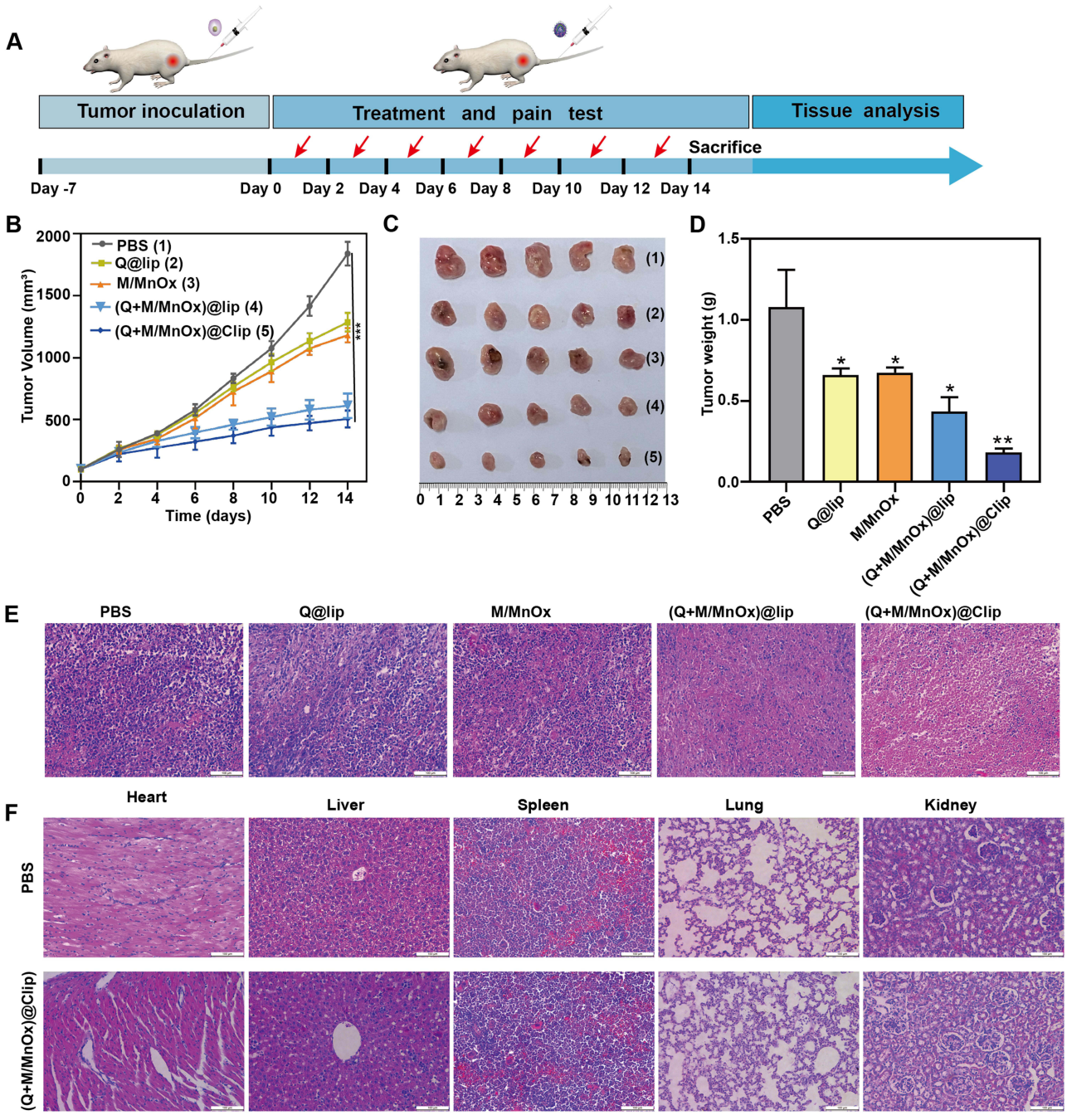

Figure 7 (Q+M/MnOx)@Clip inhibited tumor growth in vivo. (**A**) Schematic of the treatment protocol in mice. (**B**) Tumor volume curves (mean ± SD, n = 5, ***, $P < 0.001$ vs the PBS group). (**C**) Photos of tumors. (**D**) Tumor weights (mean ± SD, n = 5, *, $P < 0.05$, **, $P < 0.01$ vs the PBS group). (**E**) H&E-stained section of the tumor (bar = 100μm). (**F**) H&E-stained liver, spleen, kidney, heart, and lung (bar = 100 μm).

https://doi.org/10.2147/IJN.S523754

Following the treatment protocol, the mice were euthanized through cervical dislocation. Tumors were extracted from the animals and subjected to photographic documentation (Figure 7C). The weight variations of the tumors within each experimental group were assessed (Figure 7D). Histological examinations revealed profound nuclear condensation and a notable decrease in cell count within the (Q+M/MnOx)@Clip group, confirming the induction of apoptosis (Figure 7E). These observations once again affirmed the ability of (Q+M/MnOx)@Clip to significantly impede tumor growth. Throughout the treatment period, no significant disparities in body weights were discerned among the groups (Figure S7). Posttreatment evaluations of H&E-stained tissue sections from the heart, liver, spleen, lungs, and kidneys failed to reveal any notable differences between the PBS group and the (Q+M/MnOx)@Clip group, underscoring the therapeutic biosafety of the biomimetic liposome (Figure 7F).

(Q+M/MnOx)@Clip-Mediated Immune Responses in vivo

The M/MnOx incorporated within the (Q+M/MnOx)@Clip interacts with endogenous H_2O_2 and H^+, catalyzing the conversion into O_2 and Mn^{2+}, which effectively alleviates the hypoxic and acidic characteristics of TME while concurrently bolstering the tumor immune response. After verifying the capacity of (Q+M/MnOx)@Clip to elicit ICD and accelerate DC maturation in vitro, we performed the in vivo assessment of its antitumor immune response. FCM revealed a marked augmentation in the DC population within the mouse lymph nodes, accompanied by the elevated expression of maturation markers CD80 and CD86 (Figures 8A and S8A), indicating that (Q+M/MnOx)@Clip promotes the maturation and activation of DC.

Mature DCs are adept at activating $CD4^+$ and $CD8^+$ T cells.[15] The results demonstrated that the blood of mice treated with (Q+M/MnOx)@Clip exhibited notably elevated levels of $CD4^+$ T and $CD8^+$ T cells compared with those in the other groups, conclusively demonstrating that (Q+M/MnOx)@Clip was highly effective in activating T cells and subsequently bolstering the human immune response (Figures 8B–C and S8B and C). IHC analysis of tumor sections unveiled an enhancement in the infiltration of $CD4^+$T and $CD8^+$T cells within the tumor tissues of the mice treated with (Q+M/MnOx)@Clip (Figure 8D–E).

Evaluation of Cancer Pain Relief in vivo

At 7 days post-inoculation of 4T1 cells into the mice, surgical dissection was performed to anatomize the tumor site along with the sciatic nerves bilaterally. The diameter of the left tumor-proximal sciatic nerve was significantly reduced compared with that of its contralateral counterpart (Figure 9A), demonstrating the successful establishment of the cancer pain model. We continuously monitored mechanical and thermal hyperalgesia in the tumor-bearing mice. Compared with those in the PBS group, the mechanical and thermal pain thresholds in the Q@lip, M/MnOx, (Q+M/MnOx)@lip, and (Q+M/MnOx)@Clip groups were notably elevated (Figure 9B and C). The most pronounced increase was observed in the (Q+M/MnOx)@Clip group, suggesting that this formulation can significantly alleviate pain in mice and demonstrating its superior efficacy over the other tested groups. In addition, the (Q+M/MnOx)@Clip treatment group exhibited a notable decrease in HIF-1α and VEGF-A levels within the tumor tissues (Figures 9D–F and S9). The results supported that (Q+M/MnOx)@Clip achieved a dual effect of inhibiting tumor growth and curbing the secretion of VEGF-A from the tumor into the bloodstream, further leading to the mitigation of tumor-induced pain.

Discussion

TNBC exhibits particular aggressiveness and drug resistance, significantly narrowing the scope of treatment options posing a serious threat to women's life and health.[30] VEGF-A involves in both cell proliferation and cancer pain of patients.[4] Here, this study developed a novel nano-herb delivery system of exceptional targeting proficiency and herb delivery toward homologous cancer cells. In this system, (Q+M/MnOx)@lip was crafted through thin-film hydration by incorporating soybean lecithin, cholesterol, Q, and M/MnOx in a mass ratio of 36.1: 9.5: 4.5: 4.5, with Q encapsulated within a phospholipid bilayer and M/MnOx seamlessly integrated into its hydrophilic core. Sourced from 4T1 cells, the cancer cell membrane was extracted and subsequently fused with the prefabricated (Q+M/MnOx)@lip under water bath ultrasound, achieving integration between the membrane and the phospholipid bilayer. Our results demonstrated that this system exhibits in anti-tumor immunity and pain relief for TNBC therapy.

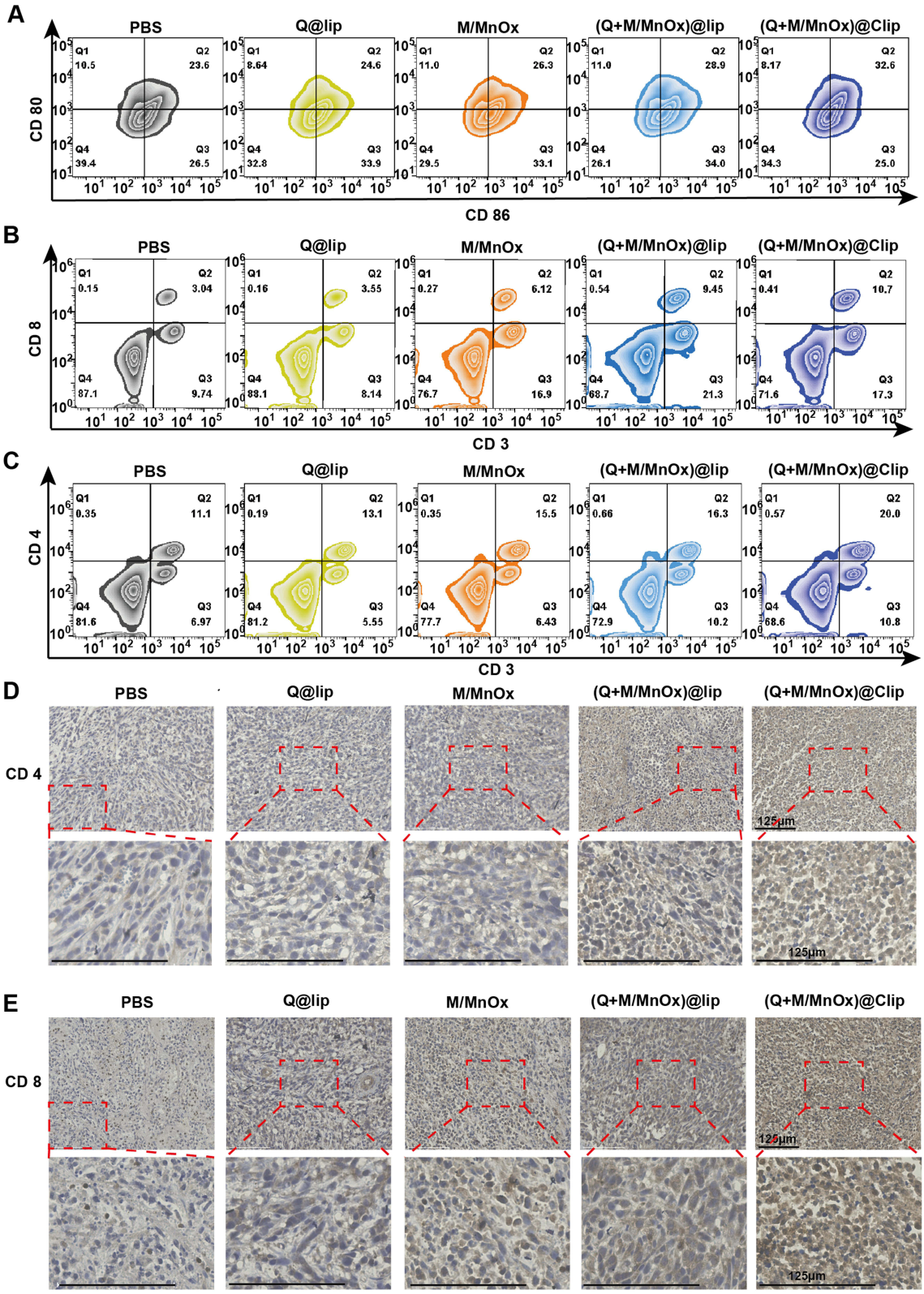

Figure 8 Nanoparticles-mediated immune responses in vivo. (**A**) DC maturation state markers CD86 and CD80 were detected using FCM. (**B**) FCM analysis of $CD8^+$ and (**C**) $CD4^+$ T cell expression profiles in blood. (**D**) IHC staining of CD4 (bar = 125 μm). (**E**) IHC staining of CD8 (bar = 125 μm).

https://doi.org/10.2147/IJN.S523754

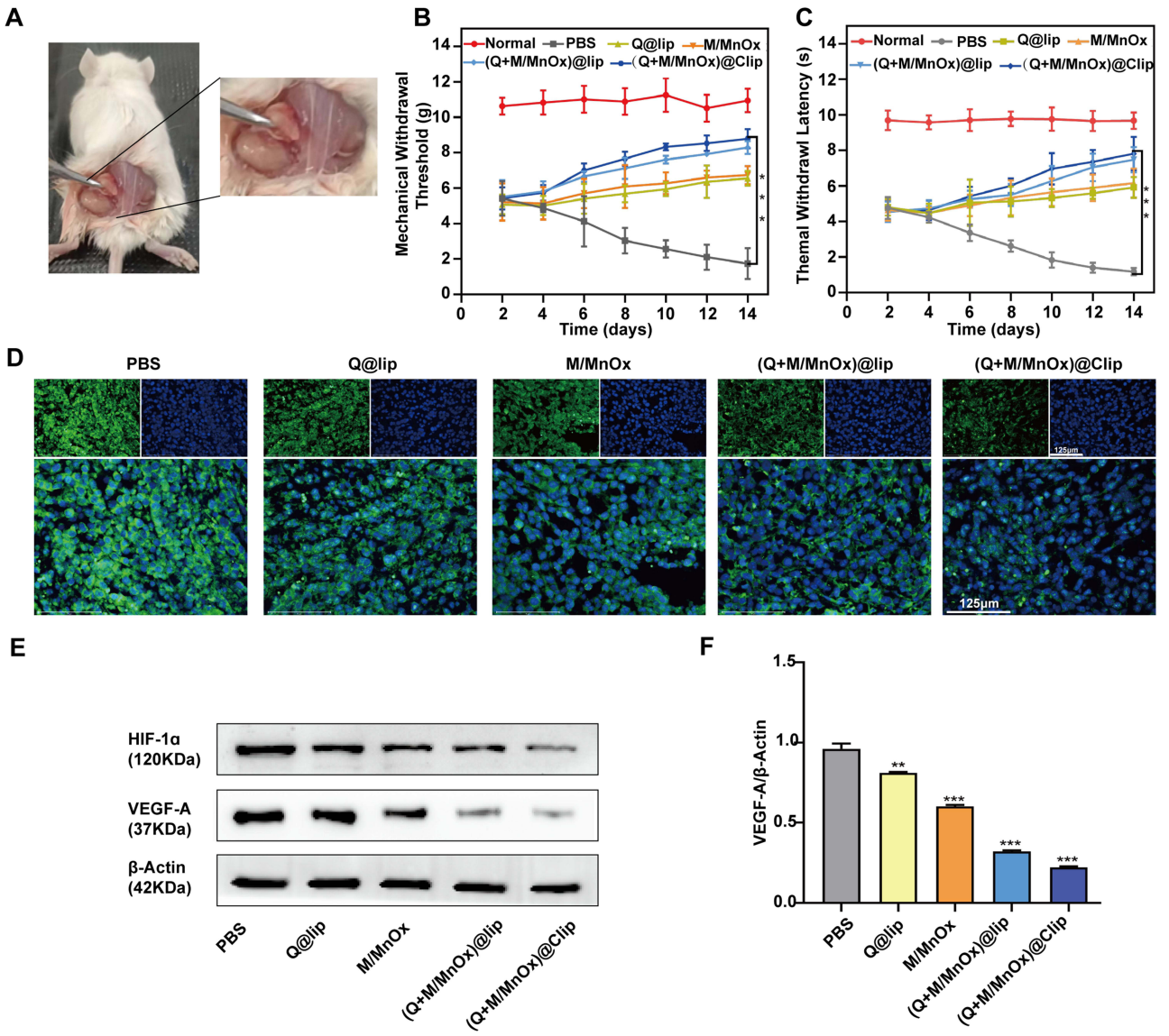

Figure 9 Particles reduced the tumor-induced pain. (**A**) Establishment of cancer pain mouse model. (**B**) MWT value. (**C**) TWL value. (**D**) IF staining of tumor tissues showing VEGF-A expression (green) and cell nuclei stained with DAPI (blue) (bar = 125 μm). (**E**) HIF-1α and VEGF-A expression levels were analyzed by WB. (**F**) WB quantification of VEGF-A. (mean ± SD, n = 3, **, $P < 0.01$, ***, $P < 0.001$ vs the PBS group).

Cancer cell membrane biomimetic technology has attracted significant attention due to its unique ability to integrate the outer layer characteristics of cancer cell membranes into the surface of nanoparticles, endowing the latter with external "markers" that are similar to actual cancer cells.[31] Such biomimetic nanoparticles can significantly enhance targeting and recognition capabilities in biological bodies by leveraging the biological properties of cancer cell surfaces.[32] Given that liposomes are a well-established drug delivery system with a membrane structure highly similar to cancer cell membranes, the fusion of homologous cancer cell membranes with liposome membranes can create a biomimetic liposome nanosystem with homologous targeting capabilities.[15,33] In the present study, the fusion of 4T1 cell membranes with liposomal structures was designed to integrate the homologous targeting capability conferred by tumor cell membranes with the drug delivery efficiency and structural stability provided by liposomes. This hybrid configuration enhances tumor-specific accumulation by combining passive targeting through the enhanced permeability and retention effect and active homotypic binding to 4T1 TNBC cells, thereby optimizing therapeutic delivery. In addition, the incorporation of cancer cell membrane biomimetic technology not only significantly enhances the targeting and recognition capabilities of nanoparticles within biological systems, but also elevates their performance in drug delivery and bioavailability of natural extracts in vivo.[34] Therefore, we designed the (Q+M/MnOx)@Clip fusing breast cancer cell membranes with liposome, which promotes the efficacy of

biomimetic liposomes in facilitating and enhancing the uptake by homologous tumor targeting. Furthermore, the pH 7.4 and pH 5.5 conditions used in the release study was designed to mimic the physiological environment and the acidic conditions of TME, respectively. The enhanced release at acidic pH aligns with the known Warburg effect, where cancer cells exhibit an acidic extracellular milieu due to elevated glycolysis.

Mitigating hypoxia within the TME is paramount for efficacious tumor therapy.[35] The M/MnOx nanoparticles can exhibit a dual-pronged approach within the TME, generating O_2 and •OH radicals.[36] This process diminishes VEGF-A expression by mitigating tumor hypoxia and exerts a potent cytotoxic effect via chemical kinetics. Q was reported that effectively inhibits tumor growth and metastasis by curbing VEGF levels through the suppression of the HIF-1α/VEGF-A pathway, thus impeding the development and abnormal proliferation of tumor blood vessels.[37] In vivo elimination of (Q+M/MnOx)@Clip nanoparticles are key for clinical translation. Biodegradable manganese oxide nanomaterials have been shown to dissolve under physiological conditions, enabling clearance via the liver or kidneys. These pathways may help safely eliminate our nanoparticles and reduce long-term toxicity. Further pharmacokinetic studies are needed to confirm their distribution and clearance. Thereafter, the efficacy of (Q+M/MnOx)@Clip in improving the TME and activating the immune response was explored in this study, focusing on hypoxia alleviation, VEGF-A expression modulation, and immune system activation. Our results showed that the (Q+M/MnOx)@Clip can facilitate the expedited release of Q, which further alleviate hypoxia, and reduced HIF-1α and VEGF-A expression in vitro and in vivo.

The HIF-1α/VEGF pathway not only plays a crucial role in tumorigenesis but is also closely associated with tumor cell drug resistance. Under hypoxic conditions, HIF-1α can activate a variety of downstream proteins involved in angiogenesis and drug resistance, such as VEGF, P-glycoprotein, breast cancer resistance protein, and multidrug resistance-associated proteins.[38] These proteins contribute to abnormal vascularization and enhance drug efflux, thereby promoting tumor cell drug resistance. Downregulation of HIF-1α and its downstream targets, including VEGF and resistance-associated transporters, not only restores tumor sensitivity to chemotherapy and targeted therapies but also improves treatment outcomes. Notably, inhibition of VEGF can remodel tumor vasculature, enhance drug delivery, and suppress hypoxia-driven adaptive responses. Interestingly, preclinical models of EGFR-mutant non-small cell lung cancer have demonstrated that VEGF blockade synergizes with EGFR-targeted therapy, significantly inhibiting tumor growth and delaying the onset of resistance.[39] Therefore, Inhibition of HIF-1α/VEGF pathway by nano-herb delivery system in this study would provide a new therapeutic approach for tumor cell drug resistance.

Cancer immunotherapy, by virtue of its remarkable capacity to effectively activate and rejuvenate the anti-tumor immune response within the body, thereby establishing long-lasting and potent immune surveillance, has ushered in a novel paradigm in cancer treatment.[40] Among the promising candidates in this field, melanin, a ubiquitous natural biopolymer prevalent in various organisms including human skin, stands out due to its inherent properties, vast biological functionalities, and distinctive physicochemical and biological characteristics, garnered from natural occurrence and extraction from living organisms.[41,42] With these unique attributes, melanin shows potential to induce ICD and consequently activate a potent anti-tumor immune response, paving the way for effective cancer therapies.[13,43] We found that the (Q+M/MnOx)@Clip can effectively deliver the melanin into TNBC cells.

Manganese oxide nanoparticles can transform the immunosuppressive TME by interacting with endogenous H_2O_2/H^+ to generate O_2 and Mn^{2+}, thus alleviating hypoxic and acidic tumor conditions.[35,44] They also adeptly produce harmful hydroxyl radicals (•OH) and superoxide ($•O_2-$) radicals, initiating Fenton-like reactions for enhanced chemodynamic therapy (CDT).[36] CDT efficiently eliminates tumor cells while triggering ICD, thereby activating the adaptive immune response of the body.[37,45] Our results also showed that (Q+M/MnOx)@Clip can enhance the generation of •OH and ROS, and the ROS surge imparted the capability to induce cytotoxic effects on tumor cells, ultimately prompting ICD and stimulating an antitumor immune response.[46] We further investigated the ICD to evaluate the anti-tumor immune response, and found that the nanoparticles lead to a notable augmentation in the secretion of DAMPs (HMGB1, ATP, and CRT) in they-treated 4T1 cells. These DAMPs are liberated during necrosis or apoptosis of tumor cells, potently enhance DC maturation. To evaluate DC maturation, we cocultured a range of nanomaterials with 4T1 cells for 24 h and utilized the bioactive molecule-rich supernatants from these cultures to stimulate induced bone marrow-derived DC. Our results showed that (Q+M/MnOx)@Clip group demonstrated substantial enhancement in DC maturation in vitro and in vivo, indicating that (Q+M/MnOx)@Clip promotes the maturation and activation of DC.

Mature DCs are adept at activating $CD4^+$ and $CD8^+$ T cells, leading to a pronounced elevation in their abundance within the bloodstream and tissues. In turn, this increased abundance significantly amplifies the human immune response.[47,48] IHC analysis of tumor sections unveiled an enhancement in the infiltration of $CD4^+$T and $CD8^+$T cells within the tumor tissues of the mice treated with (Q+M/MnOx)@Clip, supported that it activates T cells in the peripheral circulation and orchestrates the migration and infiltration of vital immune cells directly to the TME, thereby potentiating the anti-tumor immune response.

The O_2 produced through the interaction of M/MnOx and endogenous H_2O_2/H^+ effectively downregulates HIF-1α expression and subsequently diminishes VEGF-A levels, collectively contributing to the alleviation of cancer pain.[49,50] The mechanical and thermal pain thresholds were notably elevated and the HIF-1α and VEGF-A levels were decreased within the tumor tissues in the (Q+M/MnOx)@Clip groups, indicating that these nanoparticles achieved a dual effect of inhibiting tumor growth and alleviating tumor-induced pain. While our current findings highlight the pivotal role of the HIF-1α/VEGF axis, future studies will investigate additional components of this pathway, including PI3K/Akt/mTOR signaling proteins, to fully elucidate the molecular mechanisms underlying the anti-tumor effect of (Q+M/MnOx)@Clip. The use of opioid drugs is accompanied by a series of side effects, such as nausea, vomiting, and reduced response (ie, habituation), which limit their long-term effectiveness.[51] The application of this nano-herb system may overcoming the series of side effects of opioid drugs. The combined T1-weighted imaging capability of melanin and MnOx in MRI significantly can also enhance the accuracy and efficiency of tumor diagnosis.[14,52] Our study showed that T1-weighted MRI images of (Q+M/MnOx)@Clip at varying concentrations and T1-weighted MRI scans in tumor-bearing mice, confirming the MRI capability of (Q+M/MnOx)@Clip. Moreover, considering that selective cytotoxicity remains a major challenge in cancer drug development, further research should focus on the cytotoxicity of this delivery system on different cell types.

Conclusion

Oxygen-generating biomimetic nano-herb delivery system (Q+M/MnOx)@Clip were developed to elicit immune responses and enable CDT, thereby achieving synergistic cancer therapy and pain relief. This nanodelivery system can effectively suppress TNBC cell growth and enhance the effectiveness of immunotherapy in vitro and in vivo. In addition, it demonstrated T1-weighted imaging capability, enabling image-guided precision therapy against TNBC. Importantly. (Q+M/MnOx)@Clip reduced VEGF-A levels, offering strategies to alleviate cancer-related pain. Therefore, this oxygen-generating biomimetic nano-herb delivery system holds potential for targeted tumor immunization and CDT combined therapy, revolutionizing cancer treatment and offering hope to patients suffering from TNBC and associated pain.

Abbreviations

ATP, Adenosine triphosphate; BC, Breast cancer; CDT, Chemodynamic therapy; CRT, calreticulin; DAMPs, damage-associated molecular patterns; DMEM, Dulbecco's modified Eagle's medium; DLS, dynamic light scattering; DCFDA, 2,7-Dichlorofluorescein diacetate; ELISA, enzyme-linked immunosorbent assay; FCM, Flow Cytometry; HMGB1, High mobility group box-1 protein;HIF-1α, hypoxia-inducible factor-1α; ICD, immunogenic cell death; IHC, immunohistochemistry; $KMnO_4$, potassium permanganate;MnOx, manganese oxide; MWT, mechanical withdrawal threshold;MB, methylene blue; MRI, magnetic resonance imaging; PBS, phosphate-buffered saline; PDI, polydispersion index; Q, Quercetin; ROS, Reactive Oxygen Species; SDS-PAGE, sodium dodecyl sulfate-polyacrylamide gel electrophoresis; TNBC, triple-negative breast cancer; TWL, thermal withdrawal latency; TAAs, tumor-associated antigens; TEM, transmission electron microscopy; VEGF-A, vascular endothelial growth factor A; WB, Western blot; XPS, X-ray photoelectron spectroscopy.

Acknowledgments

We thank professional editing support from https://www.ShineWrite.com (service@shinewrite.com) for editing the English text of a draft of this manuscript. We created schematic illustration of in vivo study using the Adobe Illustrator software.

Funding

The present study was supported by the Special Project for Traditional Chinese Medicine Technological Innovation Project of Binzhou Medical University (No. 2024ZYYZX02), Yantai Science and Technology Innovation Development Program-Basic Research Project (2024JCYJ089), Shandong Province Medical and Health Science and Technology

Project (202413020215), National Natural Science Foundation of China (No.81772281, 31371321), the Natural Science Foundation of Shandong (No. ZR2022LSW002, ZR2024MH228), the Education Department of Shandong Province (2021KJK005, 2022KJ091), and the Science Fund of Shandong Laboratory of Advanced Materials and Green Manufacturing (Yantai) (AMGM2023F16).

Disclosure

The authors report no conflicts of interest in this work.

References

1. Ashrafizadeh M, Zarrabi A, Bigham A, et al. (Nano)platforms in breast cancer therapy: drug/gene delivery, advanced nanocarriers and immunotherapy. *Med Res Rev*. 2023;43(6):2115–2176. doi:10.1002/med.21971
2. Derakhshan F, Reis-Filho JS. Pathogenesis of Triple-Negative Breast Cancer. *Ann Rev Pathol*. 2022;17(1):181–204. doi:10.1146/annurev-pathol-042420-093238
3. Ji J, Guo J, Chi Y, Su F. Cancer Pain Management with Traditional Chinese Medicine: current Status and Future Perspectives. *Am J Chin Med*. 2024;52(1):123–135. doi:10.1142/s0192415x24500058
4. Zhang J, Zhu S, Tan Q, et al. Combination therapy with ropivacaine-loaded liposomes and nutrient deprivation for simultaneous cancer therapy and cancer pain relief. *Theranostics*. 2020;10(11):4885–4899. doi:10.7150/thno.43932
5. Lai WF, Wong WT. Design and optimization of quercetin-based functional foods. *Crit Rev Food Sci Nutr*. 2022;62(26):7319–7335. doi:10.1080/10408398.2021.1913569
6. Abdel Shaheed C, Hayes C, Maher CG, et al. Opioid analgesics for nociceptive cancer pain: a comprehensive review. *Ca a Cancer J Clinicians*. 2024;74(3):286–313. doi:10.3322/caac.21823
7. Britti D, Crupi R, Impellizzeri D, et al. A novel composite formulation of palmitoylethanolamide and quercetin decreases inflammation and relieves pain in inflammatory and osteoarthritic pain models. *BMC Vet Res*. 2017;13(1):229. doi:10.1186/s12917-017-1151-z
8. Fang JY, Huang KY, Wang TH, et al. Development of nanoparticles incorporated with quercetin and ACE2-membrane as a novel therapy for COVID-19. *J Nanobiotechnol*. 2024;22(1):169. doi:10.1186/s12951-024-02435-2
9. Wang Y, Li C, Wan Y, et al. Quercetin-Loaded Ceria Nanocomposite Potentiate Dual-Directional Immunoregulation via Macrophage Polarization against Periodontal Inflammation. *Small*. 2021;17(41):e2101505. doi:10.1002/smll.202101505
10. Jia Y, Yao Y, Fan L, et al. Tumor microenvironment responsive nano-herb and CRISPR delivery system for synergistic chemotherapy and immunotherapy. *J Nanobiotechnol*. 2024;22(1):346. doi:10.1186/s12951-024-02571-9
11. Yang C, Ming H, Li B, et al. A pH and glutathione-responsive carbon monoxide-driven nano-herb delivery system for enhanced immunotherapy in colorectal cancer. *J Control Rel*. 2024;376:659–677. doi:10.1016/j.jconrel.2024.10.043
12. Han X, Gong C, Yang Q, Zheng K, Wang Z, Zhang W. Biomimetic Nano-Drug Delivery System: an Emerging Platform for Promoting Tumor Treatment. *Int J Nanomed*. 2024;19:571–608. doi:10.2147/ijn.S442877
13. Guo K, Jiao Z, Zhao X, Hu Y, Zhao N, Xu FJ. Melanin-Based Immunoregulatory Nanohybrids Enhance Antitumor Immune Responses in Breast Cancer Mouse Model. *ACS nano*. 2023;17(11):10792–10805. doi:10.1021/acsnano.3c02287
14. Liang Y, Wang PY, Li YJ, et al. Multistage O(2)-producing liposome for MRI-guided synergistic chemodynamic/chemotherapy to reverse cancer multidrug resistance. *Int J Pharm*. 2023;631:122488. doi:10.1016/j.ijpharm.2022.122488
15. Zhang W, Gong C, Chen Z, Li M, Li Y, Gao J. Tumor microenvironment-activated cancer cell membrane-liposome hybrid nanoparticle-mediated synergistic metabolic therapy and chemotherapy for non-small cell lung cancer. *J Nanobiotechnol*. 2021;19(1):339. doi:10.1186/s12951-021-01085-y
16. Cheng L, Zhang X, Tang J, Lv Q, Liu J. Gene-engineered exosomes-thermosensitive liposomes hybrid nanovesicles by the blockade of CD47 signal for combined photothermal therapy and cancer immunotherapy. *Biomaterials*. 2021;275:120964. doi:10.1016/j.biomaterials.2021.120964
17. Zhao P, Wang S, Jiang J, et al. Targeting lactate metabolism and immune interaction in breast tumor via protease-triggered delivery. *J Control Rel*. 2023;358:706–717. doi:10.1016/j.jconrel.2023.05.024
18. Lin LS, Song J, Song L, et al. Simultaneous Fenton-like Ion Delivery and Glutathione Depletion by MnO(2) -Based Nanoagent to Enhance Chemodynamic Therapy. *Angew Chem Int Ed Engl*. 2018;57(18):4902–4906. doi:10.1002/anie.201712027
19. Ding B, Zheng P, Jiang F, et al. MnO(x) Nanospikes as Nanoadjuvants and Immunogenic Cell Death Drugs with Enhanced Antitumor Immunity and Antimetastatic Effect. *Angew Chem Int Ed Engl*. 2020;59(38):16381–16384. doi:10.1002/anie.202005111
20. Shimoyama M, Tatsuoka H, Ohtori S, Tanaka K, Shimoyama N. Change of dorsal horn neurochemistry in a mouse model of neuropathic cancer pain. *Pain*. 2005;114(1–2):221–230. doi:10.1016/j.pain.2004.12.018
21. Zhang J, Zhu S, Zhao M, et al. Analgesic and potentiated photothermal therapy with ropivacaine-loaded hydrogels. *Theranostics*. 2023;13(7):2226–2240. doi:10.7150/thno.81325
22. Amash A, Wang L, Wang Y, et al. CD44 Antibody Inhibition of Macrophage Phagocytosis Targets Fcγ Receptor- and Complement Receptor 3-Dependent Mechanisms. *J Iimmunol*. 2016;196(8):3331–3340. doi:10.4049/jimmunol.1502198
23. Gonzalez-Avila G, Sommer B, Flores-Soto E, Aquino-Galvez A. Hypoxic Effects on Matrix Metalloproteinases' Expression in the Tumor Microenvironment and Therapeutic Perspectives. *Int J Mol Sci*. 2023;24(23):16887. doi:10.3390/ijms242316887
24. Li X, Gao Y, Liu X, et al. Ultrasound and laser-promoted dual-gas nano-generator for combined photothermal and immune tumor therapy. *Front Bioeng Biotechnol*. 2022;10:1005520. doi:10.3389/fbioe.2022.1005520
25. Wang L, Wu H, Xiong L, et al. Quercetin Downregulates Cyclooxygenase-2 Expression and HIF-1 α /VEGF Signaling-Related Angiogenesis in a Mouse Model of Abdominal Aortic Aneurysm. *Biomed Res Int*. 2020;2020(1):9485398. doi:10.1155/2020/9485398
26. Qiao W, Chen J, Zhou H, et al. A Single-Atom Manganese Nanozyme Mn-N/C Promotes Anti-Tumor Immune Response via Eliciting Type I Interferon Signaling. *Adv Sci*. 2024;11(14):e2305979. doi:10.1002/advs.202305979

27. Zheng L, Li C, Huang X, et al. Thermosensitive hydrogels for sustained-release of sorafenib and selenium nanoparticles for localized synergistic chemoradiotherapy. *Biomaterials*. 2019;216:119220. doi:10.1016/j.biomaterials.2019.05.031
28. Galluzzi L, Vitale I, Warren S, et al. Consensus guidelines for the definition, detection and interpretation of immunogenic cell death. *J Immuno Ther Cancer*. 2020;8(1):e000337. doi:10.1136/jitc-2019-000337
29. Fang RH, Gao W, Zhang L. Targeting drugs to tumours using cell membrane-coated nanoparticles. *Nat Rev Clin Oncol*. 2023;20(1):33–48. doi:10.1038/s41571-022-00699-x
30. So JY, Ohm J, Lipkowitz S, Yang L. Triple negative breast cancer (TNBC): non-genetic tumor heterogeneity and immune microenvironment: emerging treatment options. *Pharmacol Ther*. 2022;237:108253. doi:10.1016/j.pharmthera.2022.108253
31. Yang R, Xu J, Xu L, et al. Cancer Cell Membrane-Coated Adjuvant Nanoparticles with Mannose Modification for Effective Anticancer Vaccination. *ACS nano*. 2018;12(6):5121–5129. doi:10.1021/acsnano.7b09041
32. Chen Z, Zhao P, Luo Z, et al. Cancer Cell Membrane-Biomimetic Nanoparticles for Homologous-Targeting Dual-Modal Imaging and Photothermal Therapy. *ACS nano*. 2016;10(11):10049–10057. doi:10.1021/acsnano.6b04695
33. Duan M, Zhou D, Ke J, et al. Dual targetable drug delivery system based on cell membrane camouflaged liposome for enhanced tumor targeting and improved anti-tumor efficiency. *Colloids Surf B*. 2024;238:113892. doi:10.1016/j.colsurfb.2024.113892
34. Kim HY, Kang M, Choo YW, et al. Immunomodulatory Lipocomplex Functionalized with Photosensitizer-Embedded Cancer Cell Membrane Inhibits Tumor Growth and Metastasis. *Nano Lett*. 2019;19(8):5185–5193. doi:10.1021/acs.nanolett.9b01571
35. Duan J, Zhao S, Duan Y, et al. Mno(x) Nanoenzyme Armed CAR-NK Cells Enhance Solid Tumor Immunotherapy by Alleviating the Immunosuppressive Microenvironment. *Advanced healthcare materials*. *Adv Healthcare Mater*. 2024;13(11):e2303963. doi:10.1002/adhm.202303963
36. Zhang K, Ma Z, Li S, et al. Platelet-Covered Nanocarriers for Targeted Delivery of Hirudin to Eliminate Thrombotic Complication in Tumor Therapy. *ACS nano*. 2022;16(11):18483–18496. doi:10.1021/acsnano.2c06666
37. Zhao Z, Dong S, Liu Y, et al. Tumor Microenvironment-Activable Manganese-Boosted Catalytic Immunotherapy Combined with PD-1 Checkpoint Blockade. *ACS nano*. 2022;16(12):20400–20418. doi:10.1021/acsnano.2c06646
38. Yong L, Tang S, Yu H, et al. The role of hypoxia-inducible factor-1 alpha in multidrug-resistant breast cancer. *Front Oncol*. 2022;12:964934. doi:10.3389/fonc.2022.964934
39. Nilsson MB, Robichaux J, Herynk MH, et al. Altered Regulation of HIF-1α in Naive- and Drug-Resistant EGFR-Mutant NSCLC: implications for a Vascular Endothelial Growth Factor-Dependent Phenotype. *J Thoracic Oncol*. 2021;16(3):439–451. doi:10.1016/j.jtho.2020.11.022
40. Meng L, Cheng Y, Tong X, et al. Tumor Oxygenation and Hypoxia Inducible Factor-1 Functional Inhibition via a Reactive Oxygen Species Responsive Nanoplatform for Enhancing Radiation Therapy and Abscopal Effects. *ACS nano*. 2018;12(8):8308–8322. doi:10.1021/acsnano.8b03590
41. Park J, Moon H, Hong S. Recent advances in melanin-like nanomaterials in biomedical applications: a mini review. *Biomater Res*. 2019;23(1):24. doi:10.1186/s40824-019-0175-9
42. Zhao X, Sun J, Dong J, et al. An auto-photoacoustic melanin-based drug delivery nano-platform for self-monitoring of acute kidney injury therapy via a triple-collaborative strategy. *Acta Biomater*. 2022;147:327–341. doi:10.1016/j.actbio.2022.05.034
43. Zhao X, Zhang J, Chen B, Ding X, Zhao N, Xu FJ. Rough Nanovaccines Boost Antitumor Immunity Through the Enhancement of Vaccination Cascade and Immunogenic Cell Death Induction. *Small Methods*. 2023;7(5):e2201595. doi:10.1002/smtd.202201595
44. Lu S, Feng W, Yao X, et al. Microorganism-enabled photosynthetic oxygeneration and ferroptosis induction reshape tumor microenvironment for augmented nanodynamic therapy. *Biomaterials*. 2022;287:121688. doi:10.1016/j.biomaterials.2022.121688
45. Li L, Lin Z, Xu X, et al. A pH/GSH/Glucose Responsive Nanozyme for Tumor Cascade Amplified Starvation and Chemodynamic Theranostics. *ACS App Mater Interfaces*. 2023;15(35):41224–41236. doi:10.1021/acsami.3c05412
46. Sheng Y, Li Z, Lin X, et al. In situ bio-mineralized Mn nanoadjuvant enhances anti-influenza immunity of recombinant virus-like particle vaccines. *J Control Rel*. 2024;368:275–289. doi:10.1016/j.jconrel.2024.02.027
47. Liu J, Cui Y, Cabral H, et al. Glucosylated Nanovaccines for Dendritic Cell-Targeted Antigen Delivery and Amplified Cancer Immunotherapy. *ACS nano*. 2024;18(37):25826–25840. doi:10.1021/acsnano.4c09053
48. Wang H, Mu J, Chen Y, et al. Hybrid Ginseng-derived Extracellular Vesicles-Like Particles with Autologous Tumor Cell Membrane for Personalized Vaccination to Inhibit Tumor Recurrence and Metastasis. *Adv Sci*. 2024;11(17):e2308235. doi:10.1002/advs.202308235
49. Hou Y, Shi J, Guo Y, Shi G. Inhibition of angiogenetic macrophages reduces disc degeneration-associated pain. *Front Bioeng Biotechnol*. 2022;10:962155. doi:10.3389/fbioe.2022.962155
50. Micheli L, Parisio C, Lucarini E, et al. Correction: VEGF-A/VEGFR-1 signalling and chemotherapy-induced neuropathic pain: therapeutic potential of a novel anti-VEGFR-1 monoclonal antibody. *J Experiment Clin Cancer Res*. 2024;43(1):120. doi:10.1186/s13046-024-03037-4
51. Tuhin MTH, Liang D, Liu F, et al. Peripherally restricted transthyretin-based delivery system for probes and therapeutics avoiding opioid-related side effects. *Nat Commun*. 2022;13(1):3590. doi:10.1038/s41467-022-31342-z
52. Hong ZY, Feng HY, Bu LH. Melanin-based nanomaterials: the promising nanoplatforms for cancer diagnosis and therapy. *Nanomedicine*. 2020;28:102211. doi:10.1016/j.nano.2020.102211